

Student Dust Counter: Status report at 38 AU

M. Piquette^{*,a,c}, A.R. Poppe^b, E. Bernardoni^{c,d}, J.R. Szalay^e, D. James^c, M. Horányi^{c,d}, S.A. Stern^f, H. Weaver^g, J. Spencer^f, C. Olkin^f

^a Department of Astrophysical and Planetary Science, University of Colorado Boulder, Boulder, CO, USA

^b Space Sciences Laboratory, University of California Berkeley, Berkeley, CA, USA

^c Laboratory for Atmospheric and Space Physics, Boulder, CO, USA

^d Department of Physics, University of Colorado Boulder, Boulder, CO, USA

^e Department of Astrophysical Sciences, Princeton University, NJ, USA

^f Southwest Research Institute, Boulder, CO, USA

^g Johns Hopkins University Applied Physics Laboratory, Laurel, Maryland, USA



New Horizons P&P Team

ARTICLE INFO

Keywords:

Interplanetary dust
PVDF
New Horizons
Edgeworth–Kuiper Belt

ABSTRACT

The Student Dust Counter (SDC) is an in-situ dust detector aboard the New Horizons spacecraft observing the distribution of interplanetary dust particles (IDPs) with mass $> 10^{-12}$ g or approximately $0.5 \mu\text{m}$ in radius. New Horizons was launched on January 19th, 2006 and performed a fly-by of the Pluto system on July 14th, 2015. SDC has nearly continuously mapped the dust density distribution along the trajectory of New Horizons, and it continues to operate providing measurements of the IDP in the Edgeworth–Kuiper Belt (EKB). We present results of the dust density distribution from 1 to 38 AU and compare these measurements to existing theoretical models.

1. Introduction

Information on the distribution of interplanetary dust particles (IDPs) provides constraints to the origin and evolution of planetary bodies. The distribution of IDPs depends on the sources, sinks, and dynamics of dust grains permeating the solar system. Numerical models have demonstrated that outgassing and outbursts of Jupiter Family Comets (JFCs) dominate the distribution of IDPs in the inner solar system (Nesvorný et al., 2010; Nesvorný et al., 2011) while the mutual collisions and bombardment of Edgeworth–Kuiper Belt Objects (EKBOs) by interstellar/interplanetary grains dominate the distribution of IDPs in the outer solar system (Stern, 1996; Yamamoto and Mukai, 1998; Poppe, 2015; 2016). IDPs are subject to gravity, radiation pressure, EM forces, and Poynting–Robertson drag. Under these forces, IDPs migrate inward through the solar system, often getting trapped in resonances with or scattered by the giant planets (Liou and Zook, 1999; Moro-Martín and Malhotra, 2002; Poppe, 2016). Being able to accurately map the distribution of IDPs provides insight into the parent bodies of the particles as well as the overall evolution of the solar system.

In order to observe the distribution of IDPs, several in-situ dust detectors have flown throughout the solar system on various spacecraft.

Observations of IDPs interior of Jupiter include HEOS 2 and HELIOS at Earth (Dietzel et al., 1973), Galileo at Jupiter (Grün et al., 1992b) and Ulysses above the ecliptic plane (Grün et al., 1992c). Both HEOS 2 and HELIOS flew on elliptical orbits interior of 1 AU measuring the distribution of interplanetary and interstellar dust grains (Grün et al., 1980). On its way to Jupiter, Galileo made measurements of IDPs between Venus and Jupiter for particles larger than 10^{-13} g (Grün et al., 1992a). The flux at 1.1 AU was measured to be between $(0.5 - 30) \times 10^{-5} m^{-2}s^{-1}(\pi sr)^{-1}$ depending on the spacecraft's orientation (Grün et al., 1992a). Galileo orbited Jupiter for about 8 years revealing the behavior and distribution of dust grains in the Jovian system (Krüger et al., 2001a; 2006b; 2005). Ulysses, having a similar dust instrument and mass threshold compared to Galileo, also measured the distribution of IDPs from Earth to Jupiter yielding a slightly lower dust flux at 1.1 AU of $(2.2 \pm 1.4) \times 10^{-5} m^{-2}s^{-1}(\pi sr)^{-1}$ (Grün et al., 1992a). After encountering Jupiter, Ulysses entered a highly inclined orbit enabling the observations of IDPs as a function of ecliptic latitude between 1.3 and 5.4 AU (Krüger et al., 1999; 2001b; 2006a; Krüger et al., 2010).

Observations of IDPs exterior of Jupiter have been made by the Cassini spacecraft at Saturn (Srama et al., 2004) and Pioneer 10 and 11

* Corresponding author.

E-mail address: marcus.piquette@colorado.edu (M. Piquette).

<https://doi.org/10.1016/j.icarus.2018.11.012>

Received 27 September 2017; Received in revised form 16 October 2018; Accepted 14 November 2018

Available online 15 November 2018

0019-1035/ © 2018 Elsevier Inc. All rights reserved.

extending to 9 and 18 AU, respectively (Humes, 1980). Cassini observed IDPs between Jupiter and Saturn and was able to distinguish between grains of interplanetary and interstellar origin. The flux of interstellar grains was measured to be $2 \times 10^{-5} \text{ m}^{-2}\text{s}^{-1}$ with an estimated grain size of $>4 \mu\text{m}$, agreeing with similar observations from Ulysses (Altobelli et al., 2007). Between 1 and 18 AU, the Pioneer instruments measured a near constant flux of about $(1 - 10) \times 10^{-6} \text{ m}^{-2}\text{s}^{-1}$ and $(1 - 30) \times 10^{-7} \text{ m}^{-2}\text{s}^{-1}$ for 10^{-8} and 10^{-9} g grains, respectively (Humes, 1980). In addition to dedicated dust instruments, the Voyager 1 and 2 radio and plasma wave instrument reported measurements of micron sized dust grains out to 100 AU via detections of the plasma cloud created from particles impacting the spacecraft (Gurnett et al., 1997). Both Voyager 1 and 2 measured a nearly constant flux of several detections per hour with an estimated density of $\sim 20 - 40 \text{ km}^{-3}$, however, extracting a true flux from such measurements remains challenging (Gurnett et al., 1997; 2005).

The Student Dust Counter (SDC) has mapped the dust density distribution of grains larger than 10^{-12} g along the trajectory of the New Horizons mission, now reaching past 38 AU. In-situ dust detectors provide critical information on the temporal and spatial distribution of dust in the solar system constraining modeled sources, sinks, and transport mechanisms. SDC results before New Horizons' encounter with Pluto have been reported in prior publications (Poppe et al., 2010b; Han et al., 2011; Szalay et al., 2013).

This paper is organized as follows. In Section 2 we describe the SDC instrument. Section 3 discusses SDC measurements to date and we compare them to current theoretical models of the dust density distribution in Section 4. We compare the mass distribution measured by SDC to the expectations from numerical modeling in Section 5, and discuss the results and our conclusions in Section 6.

2. Instrument description

The SDC detector panel is mounted in the ram direction of the New Horizons spacecraft. It consists of 14 permanently electrically polarized $28 \mu\text{m}$ thick polyvinylidene fluoride (PVDF) plastic film sensors, each with dimensions of $14.2 \times 6.5 \text{ cm}$ (Horányi et al., 2008). The PVDF detectors operate by detecting a change in the surface charge density on their conducting surfaces due to the cratering of the PVDF films by dust impacts (Simpson and Tuzzolino, 1985; Poppe et al., 2010a). PVDF detectors are resilient to radiation and energetic ions and electrons but exhibit pyroelectric and piezoelectric properties and are affected by temperature variations and mechanical vibrations (Simpson and Tuzzolino, 1985; Horányi et al., 2008). For this reason the instrument was designed with 2 of its 14 sensors attached to the backside of the detector panel, shielded from dust impacts (Horányi et al., 2008). The shielded detectors serve as ‘reference’ channels, providing a baseline of the noise events induced by effects other than dust impacts, including the firing of thrusters, mechanical vibrations, and random thermal electronic noise. The 12 forward facing detectors serve as ‘science’ channels, recording both dust impacts and noise events. SDC was tested and calibrated at the 2 MV Van de Graaff dust accelerator at the Max Planck Institute for Nuclear Physics in Heidelberg, Germany (James et al., 2010). Shortly after launch, one channel malfunctioned leaving only 11 active science channels.

Signals from the detector panel are processed by SDC's electronics box interior the spacecraft. Charge signals are translated into 16-bit data numbers (DN) via two analog to digital converters (ADCs) resulting in separate electronics chains, referred to as chains A and B. Chain A consists of channels 1–7 and chain B consists of channels 8–14, where channels 7 and 14 are the reference channels. SDC periodically conducts onboard tests to track electronic degradation and electronic noise. Charge stimulus tests track electronic degradation by injecting known charges at the head of each channel's electronic chain and recording the DN. Electronic noise is tracked with a noise floor test that varies the threshold on each channel over five values and the resulting

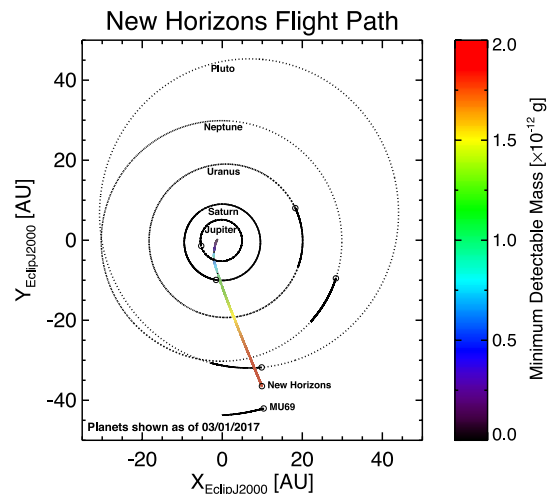


Fig. 1. The flight path of New Horizons from Earth to 38 AU. SDC observation periods are marked in color indicating the minimum mass threshold.

rate of events is recorded. Noise floor tests last between 4 min and 18 h. Based on the analysis of these tests, presented in the supplemental material, we find that SDC electronics have remained stable throughout the mission, and channels follow Poisson statistics with slightly different noise rates for the same threshold. Due to the use of two ADCs, chain A detectors display higher sensitivity to noise than chain B detectors. Also, the reference channels on chain A and B show systematically lower and higher noise rates, respectively, as compared to their corresponding science channels.

3. SDC measurements out to 38 AU

SDC has taken near continuous dust measurements from Earth to 38 AU. Fig. 1 shows New Horizons' flight path through the solar system along with SDC's minimum mass threshold. The mass threshold is set by the minimum detectable impact charge, which is a function of impact velocity (Horányi et al., 2008). As such it increases with heliocentric distance due to the decreasing speed of New Horizons.

SDC does not record full signal waveforms that could be used to identify piezoelectric and pyroelectric noise (Simpson and Tuzzolino, 1985), nor does it have a direct measure of noise for each science channel. Attempts to fit the periodic noise floor tests to estimate noise on each channel are discussed in the supplemental material. We can, however, immediately tag some events as noise due to coincidence with: (1) thruster firings; (2) stimulus test; and (3) other recorded events. Fig. 2 shows all events tagged as coincident within 1–10 s of the three sources. Typically, SDC channels are disabled around thruster firings but some operational configurations allowed SDC channels to remain enabled, such as the Pluto encounter from 31 – 33 AU and its rehearsal. Events coincident with stimulus tests, referred to as ‘stim echoes’, are much more rare and only occurred early in the mission. By far, most coincident tagged events are those coincident with other events involving many if not all channels. This is indicative of vibrations propagating through the spacecraft simultaneously triggering many channels. There was a drastic increase of coincident events after 33 AU due to a mechanical wave-guide switch associated with the spacecraft antenna that triggered all channels when used. The use of the switch was much more prevalent during the downlinking of the encounter data. Fig. 3 shows a map of all coincident tagged events and the channels it was coincident with. The coincident hits are randomly distributed with no strong correlation or ‘cross-talk’ between any two channels, although higher systematic counts are observed for chain A channels because of their higher sensitivity. There is only a $\sim 3\%$ difference between the minimum and maximum counts of the off-

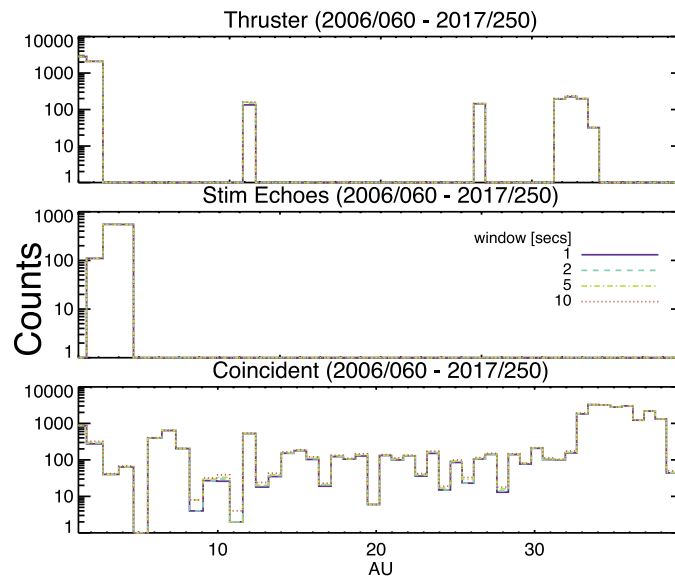


Fig. 2. History of events tagged as noise due to coincidence with: (1) thruster firings, (2) stimulus test, and (3) other recorded events. The colors and line styles indicate the time windows used to identify coincident events.

diagonal values (i.e. channels coincident with other channels). Channels that were coincident with themselves were less frequent and most likely due to persistent or larger vibrations on the spacecraft. We typically restrict data analysis to periods of spacecraft hibernation, when all other instrument and spacecraft activity is at a minimum. During all hibernation periods, SDC detector panels displayed stable temperatures varying only by a degree or two, which limits excess noise from rapid temperature variations as observed on the AIM spacecraft (Poppe et al., 2011). Additionally, we searched for coincidence between recorded events and other onboard commanding or activity. During hibernation specifically, no relation or coincidence was found.

After removing all coincident events we are left with ‘candidate hits’ made up of Poisson distributed dust impacts and electronic noise. Fig. 4 shows all recorded data excluding coincident events. SDC measures the impact charge, q_{imp} , which is a function of both the mass and the relative speed of the impacting particles (Horányi et al., 2008; James et al., 2010; Poppe et al., 2010a). The customary analysis assumes that IDPs have a mass density of 2.5 g/cm^3 and follow circular Kepler orbits, modified by radiation pressure, providing an estimate for impact speed.

Recorded noise events are given an effective charge and mass. Due to instrument noise, typical mass estimates have an error factor of ≈ 2 . The maximum mass recorded during all hibernation periods is just under $6 \times 10^{-11} \text{ g}$.

During the mission the threshold on each channel varies, so a consistent threshold must be chosen in order to directly compare dust and noise rates across channels and heliocentric distance. Fig. 5 shows the range of minimum and maximum mass thresholds for each channel during all hibernation periods. Excluding channel 11, which died shortly after launch, the maximum threshold on any channel is just below $2.5 \times 10^{-12} \text{ g}$. For this threshold, Fig. 6 shows the total counts per channel during all hibernation periods. Errors were calculated as \sqrt{N} , assuming that both dust impacts and electronic noise are Poisson distributed. The apparent disagreement between science channels is due to the difference in noise behavior integrated over all hibernation periods, totaling about 5.5 years. Given the discrepancy of noise behavior between channels, especially between chain A and B, the best estimate for noise on each science channel is assumed to be measured by its corresponding reference channel. In Fig. 6 there is a clear distinction

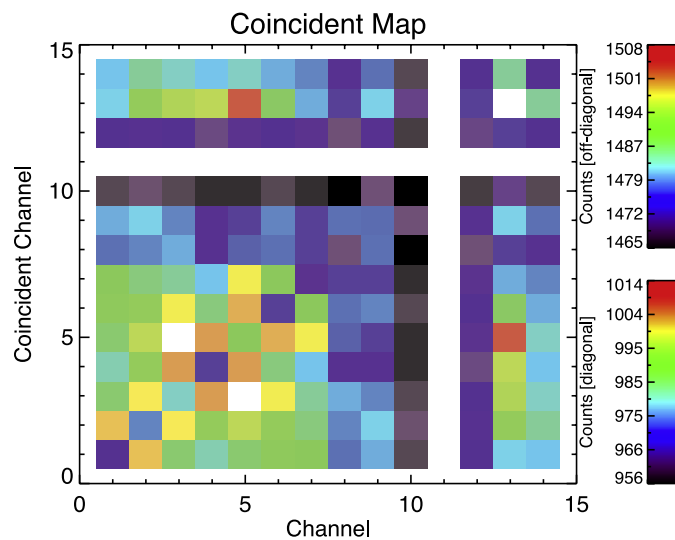


Fig. 3. Map of all coincident tagged events and the channels it was coincident with. Diagonal (i.e. channels coincident with themselves) and off-diagonal (i.e. channels coincident other channels) are shown with different color tables. Note that all channel 11 events have been omitted.

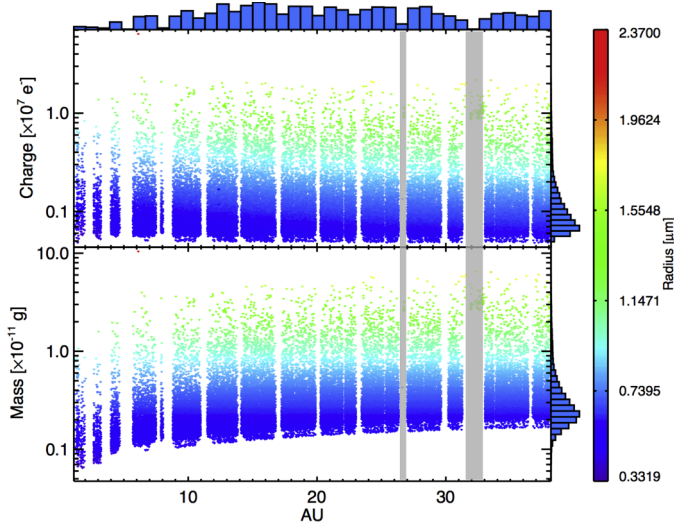


Fig. 4. The impact charges (top) and mass estimates (bottom) of all events recorded by SDC to 38 AU that were not coincident with thruster firings. Data gaps are periods when the New Horizons spacecraft transitioned to three-axis-stabilized mode and SDC was turned off. Gray bars indicate the periods of high spacecraft activity when SDC thresholds were raised during a rehearsal period and the encounter with Pluto. Blue histogram bars are included on the y and x axes. The charge threshold for detection is not changing throughout the mission but the smallest detectable charge indicates an increasing mass threshold due to the slowdown of the New Horizons spacecraft.

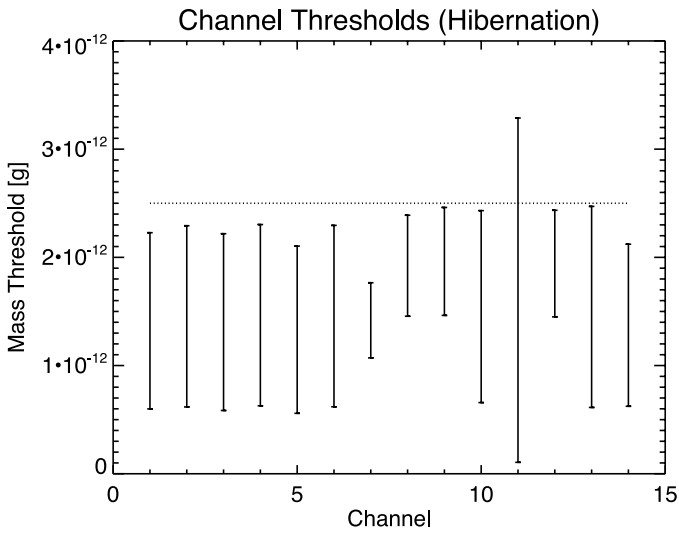


Fig. 5. Mass threshold ranges (i.e. bars show the minimum and maximum thresholds) for each channel during all hibernation periods. Shortly after launch channel 11 failed and has been removed from the data set.

between science and reference counts for the chain A detectors. This is not the case for chain B detectors, indicating that the reference channel on chain B may over estimate the noise. As discussed in the previous section, the reference channels show systematic bias such that chain A and B reference channels may under- and over-estimate noise, respectively. Fig. 7 shows the total and reduced dust counts as well as the signal to noise ratio on each channel for a single hibernation period spanning from 28.3 – 29.5 AU (~ 130 days). The reduced count on each science channel was calculated by subtracting the noise measured by its corresponding reference channel (chain A vs. chain B). The error in reduced counts was calculated by adding the error of science and reference counts in quadrature. The reduced counts on each channel are

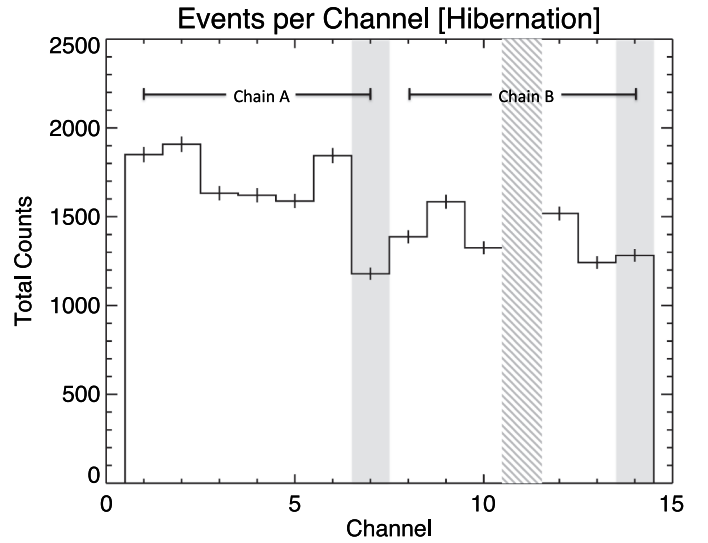


Fig. 6. Total counts per channel for events larger than 2.5×10^{-12} g over all hibernation periods. Gray bars indicate the reference channels and the striped bar indicates channel 11, which died shortly after launch. Error bars were calculated as \sqrt{N} , assuming Poisson statistic.

in better agreement but still vary due to differences in noise behavior. Furthermore, chain B detectors show systematically lower counts than chain A detectors, with channel 13 showing a negative signal to noise value. This is again attributed to our simplified assumption of using reference channels as an assumption for average noise.

The density of IDPs was derived for each hibernation period by dividing the averaged reduced dust count by the volume carved out by a single detector for both chain A and B detectors. The error on the average was taken to be the standard deviation of the reduced dust counts. The volume sampled by a single detector along any path is

$$V = A_{det} \int_{T_1}^{T_2} \hat{n}_{SDC} \cdot (\mathbf{v}_{sc} - \mathbf{v}_{dust}) dt, \quad (1)$$

where V is the volume, T_1 and T_2 are the beginning and ending times along the path, t is time, A_{det} is the area of a single detector, \hat{n}_{SDC} is the surface normal of the SDC detector panel, \mathbf{v}_{sc} is the New Horizons velocity vector, and \mathbf{v}_{dust} is the incoming dust velocity vector, given by the local Keplerian velocity. Fig. 8 shows the dust density estimate for three different size cuts at $0.6 \mu\text{m}$ ($\sim 2.5 \times 10^{-12}$ g), $0.9 \mu\text{m}$ ($\sim 7.5 \times 10^{-12}$ g), and $1.4 \mu\text{m}$ ($\sim 2 \times 10^{-11}$ g). Density estimates are shown for both chain A and B detectors separately as well as averaged. For grains $> 0.6 \mu\text{m}$, the density initially increases from 9 to 15 AU then remains fairly constant with a slight dip around 20 AU. The density then begins to increase out to the Kuiper Belt. For comparison, the plasma wave data from the Voyager spacecraft estimate IDP densities of about $20\text{--}40 \text{ km}^{-3}$ (Gurnett et al., 1997; 2005), which agrees with our estimates for the density of grains $> 0.6 \mu\text{m}$. For larger grains ($> 0.9 \mu\text{m}$), statistics become poorer but the dust density has been nearly constant, agreeing with Pioneer measurements (Humes, 1980). The higher threshold of $1.4 \mu\text{m}$ was chosen to match the thresholds used during the Pluto encounter (Bagenal et al., 2016). The increased thresholds during the encounter limited excessive noise from thruster firings while allowing SDC to remain on. A complete discussion of measurements near the Pluto system can be found in Bagenal et al. (2016), where the dust density around the Pluto system, for grains larger than $1.4 \mu\text{m}$, was estimated to be between 0.6 and 4.6 km^{-3} with a 90% confidence level.

4. Model comparisons

The distribution of IDPs in the outer solar system is dominated by dust production in the EKB (Stern, 1996; Yamamoto and Mukai, 1998;

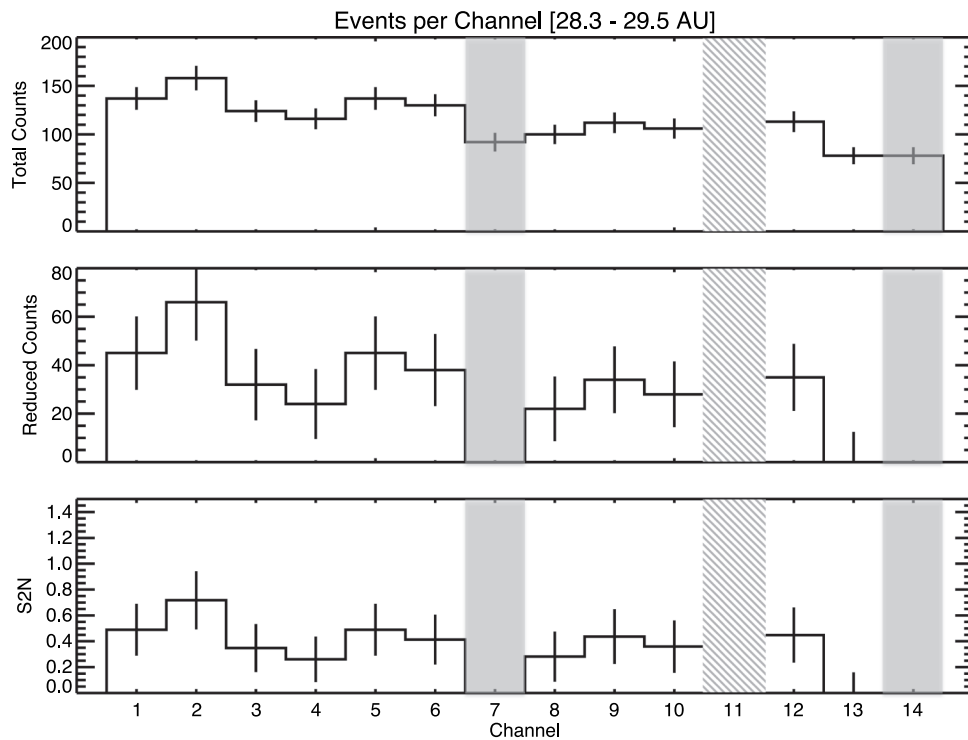


Fig. 7. Total counts, reduced counts, and signal to noise ratios per channel for events larger than 2.5×10^{-12} g over a single hibernation period. Gray bars indicate the reference channels and striped bars indicate channel 11, which died shortly after launch. Error bars were calculated as \sqrt{N} , assuming Poisson statistic.

Poppe, 2015; 2016). Dust is continually produced from EKBOs due to mutual collisions (Stern, 1996) and bombardment of interstellar and interplanetary dust (Yamamoto and Mukai, 1998; Poppe, 2015). Dust particles generated in the EKB slowly migrate towards the Sun due to Poynting-Robertson drag, and their fate is determined by possible close encounters with planets, trapping in mean motion orbital resonances (Liou et al., 1996; 1999; Moro-Martín and Malhotra, 2002; 2003), and

grain-grain collisions (Kuchner and Stark, 2010)

Recent models have detailed the sources, sinks, and transport of dust particles in the outer solar system allowing for direct comparisons with SDC observations (Vitense et al., 2012; 2014; Poppe, 2016). These models used a test particle approach, with collisional schemes introduced, integrating the motion of individual grains under the influence of gravity due to the Sun and the giant planets, radiation pressure, Poynting Robertson drag, electromagnetic perturbation due to the interplanetary magnetic fields, and grain-grain collisions. Fig. 9 shows a comparison of SDC measured flux with fitted predicted curves. These models exhibit reasonable agreement with SDC observations from 5 to 35 AU, but their predictions drastically differ for measurements penetrating further into the EKB. We note that the data used to produce the original fits assumed a smaller threshold cut of SDC data than what's presented here, resulting in slightly higher flux predictions. The models differ mainly in their treatment of grain-grain collisions, as well as the distribution of the parent bodies in the EKB; namely, Poppe (2016) included the outer EKB distribution, which extends from 48 AU out to several hundred AU and provides an extended dust source (Petit et al., 2011).

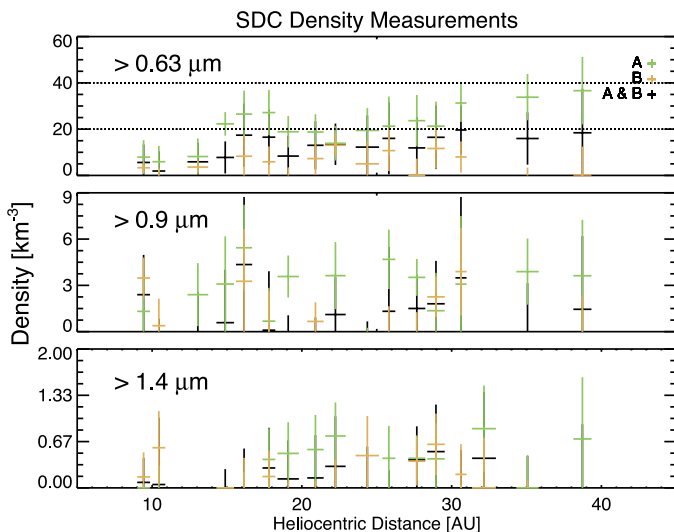


Fig. 8. Interplanetary dust density for grains with radii $>0.6 \mu\text{m}$, $>0.9 \mu\text{m}$, and $>1.4 \mu\text{m}$ estimated by chain A and B detectors separately and together. Error bars were calculated by dividing the standard deviation of the reduced counts by the sampled volume. The top panel shows estimates from the Voyager plasma wave data indicated with dashed lines. The seemingly additional point at ~ 32 AU for the largest grains is due to the inclusion of data obtained with higher thresholds around Pluto, thus no comparison is available for smaller thresholds.

In all previous analyses, the dust fluxes and densities derived from SDC measurements assumed impacting particles follow circular Kepler orbits adjusted for radiation pressure. This assumption was used to estimate the total dust production rate (Poppe, 2016) and initial size distribution in the EKB (Han et al., 2011). However, the numerical dust trajectory integrations show that particles can follow orbits with significant eccentricities and inclinations, contrary to the simplifying assumptions used in our data analysis to date. For example, Fig. 10 shows the distribution of velocity components for $0.6 - 0.85 \mu\text{m}$ grains in the range of 10 - 11 AU from the Poppe (2016) model for three distinct dust sources. Included are distributions for EKB, Jupiter Family Comet (JFC), and Oort-Cloud Comet (OCC) grains as well as the combined distribution of all three sources appropriately weighted according to the local number density as calculated by the model. EKB and JFC grains consist almost entirely of prograde orbits with JFC grains retaining a

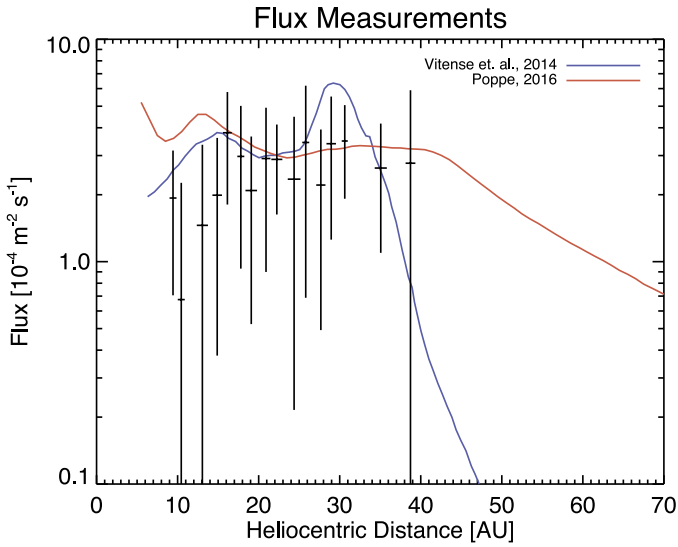


Fig. 9. Interplanetary dust flux onto SDC for grains with radii $>0.6 \mu\text{m}$. The blue (Vitense et al., 2014) and red (Poppe, 2016) curves represent two different models of the predicted dust flux. We note that the data used to produce the original fits assumed a smaller threshold cut of SDC data than what's presented here, resulting in slightly higher flux predictions. (For interpretation of the references to colour in this figure legend, the reader is referred to the web version of this article.)

larger spread in both radial and vertical velocities. OCC grains, however, are produced in highly inclined orbits and thus have populations of pro- and retrograde orbits. The combined velocity distribution is dominated by EKB grains with a total speed that peaks under the local Keplerian speed. Below we discuss our first comparisons of measured mass distribution predictions with a numerical model.

5. Mass distribution predictions

We used the most recent interplanetary dust dynamics model to compare the predicted and measured distribution of mass recorded by SDC. The model, discussed in detail in Poppe (2016), numerically integrated dust grain trajectories from four interplanetary sources. The dust sources were Halley-type comets (HTC), Oort-Cloud comets (OCC), Jupiter Family comets (JFC), and EKB Objects (EKBO) (Nesvorný et al., 2010; Landgraf et al., 2002; Poppe, 2016). Grains were assumed to be produced with a mass distribution in the form, $dM/dm \propto m^{-\alpha/3}$, where $\alpha = 2.5$. Dust sizes were represented in bins with midpoints at 0.5, 0.7, 1.0, 1.5, 2.0, 3.0, 5.0, 10.0, 15.0, 20.0, 30.0, 50.0, 70.0, 100.0 μm . For a given size bin and heliocentric distance, discretized at 1 AU intervals, the model provides a local number density, $n_{j,i}$ and three-dimensional (3D) velocity distribution in the ecliptic, $f_{j,i}(\mathbf{v}_{dust})$, where \mathbf{v}_{dust} is the dust velocity in cylindrical coordinates, j is the mass index, and i is the heliocentric distance index. Each velocity component is recorded in bins of 1 km/s in the range of ± 24 km/s.

Using the 3D velocity probability distribution, $f_{j,i}(\mathbf{v}_{dust})$, a probability distribution for impact speed and angle onto SDC, $g_{j,i}(\mathbf{v}_{imp}, \theta_{imp})$ was calculated for each dust source (i.e. EKB, OCC, and JFC). We've ignored the HTC dust source because its contributions to the IDP are insignificant compared to the other sources (Poppe, 2016). For a given \mathbf{v}_{dust} the impact speed and angle onto SDC are

$$\mathbf{v}_{imp} = \mathbf{v}_{nh} - \mathbf{v}_{dust}, \quad (2)$$

and

$$\theta_{imp} = \arccos\left(\frac{\mathbf{n}_{sdc} \cdot \mathbf{v}_{imp}}{\|\mathbf{v}_{imp}\|}\right), \quad (3)$$

where \mathbf{v}_{nh} is the spacecraft velocity and \mathbf{n}_{sdc} is the surface normal of

SDC. The corresponding probability from $f_{j,i}(\mathbf{v}_{dust})$ was then added to the appropriate speed and angle bin in $g_{j,i}(\mathbf{v}_{imp}, \theta_{imp})$. Fig. 11 shows the probability distribution of predicted impact speeds and angles onto SDC for grains with radii 0.6 - 0.85 μm in the range of 10–11 AU. OCC grains, in blue, have a wide spread in both impact speed and angle but the overall distribution, in black, is dominated by EKB grains, in green. The most probable impact angle and speed is 45° and 21 km/s, where the impact angle is measured from the detector normal. The bulk of the impact speed distribution, as predicted by the model, is smaller than the assumed circular Keplerian orbits under radiation pressure, as implemented in the SDC data analysis to date. Mass determination of SDC impact charges depend on impact velocity, which varies as $v_{imp}^{2.74}$ (James et al., 2010). From Fig. 11, the impact speeds calculated using the assumed circular orbits under radiation pressure is 22.2 km/s and the most probable speed from the full numerical model is 21 km/s, resulting in a difference in mass determination of about 15%. Given the relatively large ($\sim 100\%$) uncertainty of the mass determination of the PVDF sensors this effect remains negligible. In general, as the heliocentric distance increases, both the impact speeds and angles converge to the values calculated with the assumed circular orbits. Furthermore, deviations from the assumed circular orbits become less significant due to the increasing dominance of the spacecraft's speed.

Predicted mass distributions were calculated from the model by appropriately weighting ensembles of random impact geometries and incident grain masses. Impact geometries were weighted by the corresponding bin of the normalized distribution of impact speed and angle $g_{j,i}(\mathbf{v}_{imp}, \theta_{imp})$, calculated above. Incident masses were weighted by fitting the local densities, as reported by the model, to a power law of the form $n(m) = Cm^\delta$. For reference, Poppe (2016) used a value of $\delta = \delta_{init} = -2.5/3.0 = -0.8333$ as an initial condition in the interplanetary dust model. Note that conditions with $|\delta| < |\delta_{init}|$ indicate regions where the slope is shallower due to mass shifted towards larger grains while conditions with $|\delta| > |\delta_{init}|$ indicates regions with a steeper slope due to mass shifted towards smaller grains. Fig. 12 shows the fitted value of the power-law slope, δ , as a function of heliocentric distance for JFC grains (orange), EKB grains (green), and OCC grains (blue). The horizontal dotted line denotes the initial condition value of $\delta = \delta_{init}$.

The JFC grain power-law exponent, shown in orange, is consistently smaller than $|\delta_{init}|$, representing a relative deficit of smaller grains. Two narrow, local minima can also be seen at the orbits of Jupiter and Saturn. Overall, the shallower power-law for JFC dust grains is most likely due to the loss of small grains via radiation pressure blow-out (i.e., “beta”-meteoroids; see e.g., Zook, 1975; Zook and Berg, 1975; Wehry and Mann, 1999), leaving an overall surplus of larger grains. The high eccentricity of JFCs themselves (from which JFC grains inherit their initial orbital elements) (Levison and Duncan, 1997; Di Sisto et al., 2009) causes this to be an efficient loss process for small grains. The two local minima near Jupiter and Saturn are most likely due to the capture of smaller grains in MMRs before they can be blown out from the solar system, thereby partially restoring the local mass distribution slope closer to δ_{init} .

EKB grains, shown in green, can be roughly divided into three regions: (1) $r > 55$ AU, where $|\delta| \approx |\delta_{init}|$, (2) $30 < r < 55$ AU, where $|\delta| < |\delta_{init}|$, and $r < 30$ AU, where $|\delta| > |\delta_{init}|$. The first of these regions, $r > 55$ AU, maintains a value close to δ_{init} as dust grains generated from the EKB in the far outer solar system are not significantly perturbed by gravitational interactions with the giant planets. Regions 2 and 3, which display opposite behavior, are due to longer trapping times of larger dust grains in MMRs outside the orbit of Neptune. Thus, smaller grains can escape neptunian MMRs quicker than their larger counterparts and drift inwards through the solar system. Interestingly, these deviations in the EKB mass distribution power-law slope persist even in the face of grain-grain collisional smoothing as implemented in the model of Poppe (2016), following the methodology of Stark and Kuchner (2009).

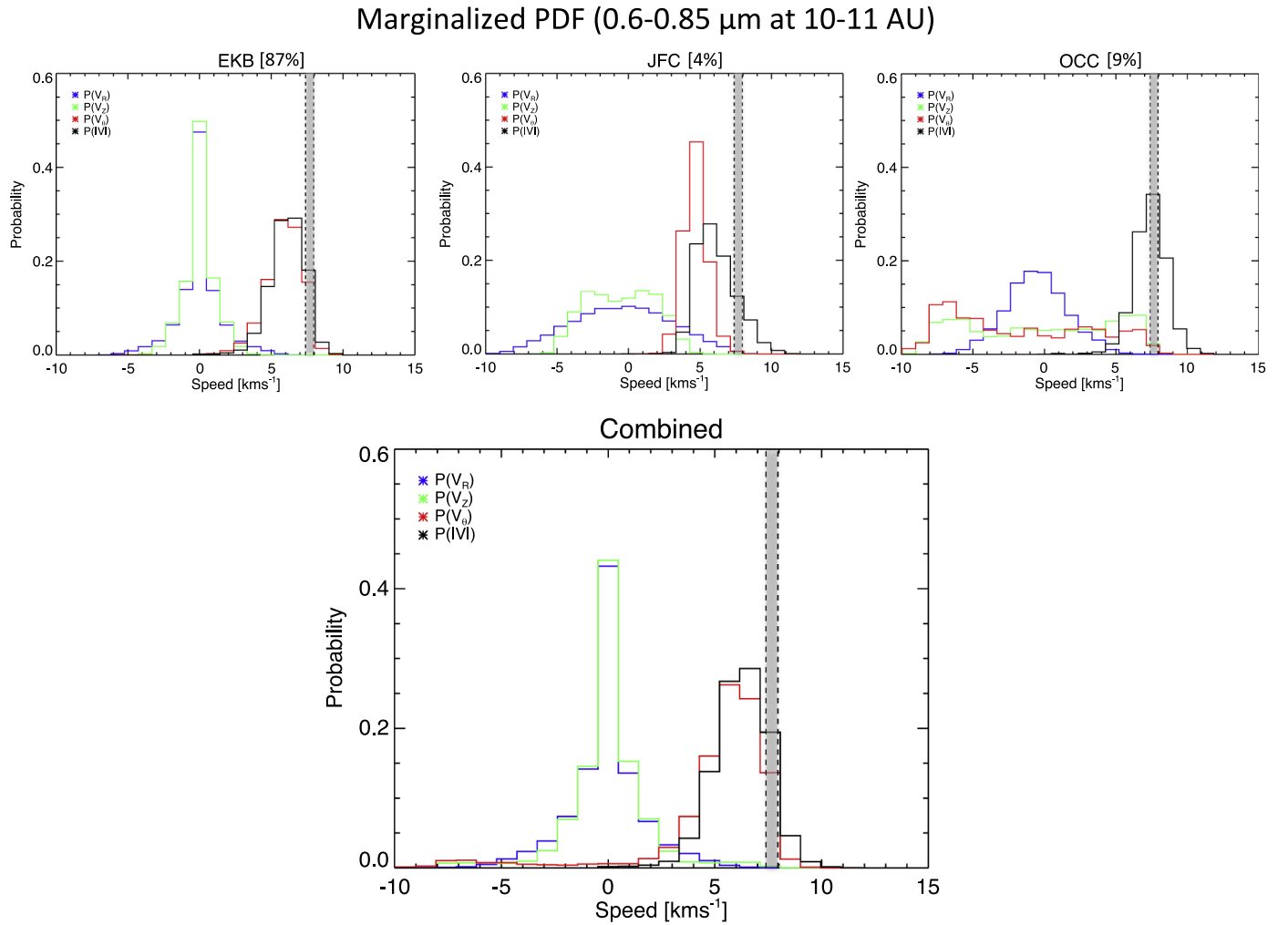


Fig. 10. Distribution of velocities for grains in the size range of 0.6–0.85 μm from 10 to 11 AU. Shown are the distributions and relative weights for JFC, OCC, and EKB grains as well as the combined distribution of all three sources properly weighted by the local density. The Kepler orbital speed for grains in this size range, including radiation pressure, are shown in gray.

Finally, OCC grains, in blue, show a large scale dichotomy in the value of δ with respect to δ_{init} . For $r > 15$ AU, $|\delta| < |\delta_{init}|$, while for $r < 15$ AU, $|\delta| > |\delta_{init}|$. The shallower slope outside 15 AU is due to the loss of beta-meteoroids, similar to JFC grains. The behavior within 15 AU is due to the so-called “Jupiter barrier”, typically discussed in the context of cometary dynamics (i.e., Duncan (2008)). For dust, such an effect appears to be size dependent (see Fig. 2, Poppe (2016)), with smaller grains able to more easily pass through the “Jupiter barrier” and diffuse into the inner solar system.

For a single dust source and heliocentric bin, 10000 ensembles of random impact geometries and incident masses were selected and properly weighted. For each ensemble, a corresponding impact charge was calculated using SDC calibrations (James et al., 2010), as well as an effective mass assuming a Kepler-like impact speed. The total weight of an ensemble was the product of the corresponding impact geometry and incident mass weights. The distribution of both incident and effective mass was then binned, normalized, and multiplied by the product of the total density reported by the model and the volume sampled by a single SDC detector described in Eqn. 1. The distributions from each source were then co-added to form predicted distributions of mass, $M_{incident}(m_{imp})$ and $M_{effective}(m_{imp})$.

Similarly, SDC measurements were binned in mass. Fig. 13 shows the reduced dust counts during all hibernation periods on each channel

for three logarithmically spaced mass bins. Chain A detectors showcase reasonable agreement across channels while chain B channels exhibit much poorer statistics, as seen in previous sections. For chain B, reduced dust counts for the middle bin are negative indicating an over estimation of the noise. Despite the poorer statistics, the average dust count for each bin was assessed in the same way as in Section 3 where chain A and B channels were analyzed separately and then averaged. Fig. 14 shows the model predicted incident and effective mass distributions as well as the distributions measured by SDC. The slight difference between the model predicted incident and effective mass distributions highlight a relatively small modification of the measured mass distribution due to assuming circular Kepler orbits. Overall, the model predicts a lower count of smaller mass grains ($< \sim 0.7 \times 10^{-11}$ g) and a higher count of larger mass grains ($> \sim 2 \times 10^{-11}$ g) than detected by SDC. In fact SDC’s measurements of particle masses $> 5 \times 10^{-11}$ g are consistent with zero detections.

Additionally, the mass distribution was analyzed for each hibernation period. For each hibernation period, the distribution of effective mass predicted by the model and measured by SDC, assuming circular Kepler orbits, were fitted with a power law. Fig. 15 shows the fitted power law index for the measured and predicted mass distributions as a function of AU. The uncertainty is taken to be the standard error of the fit. Generally, especially in the outer solar system, the model predicts a

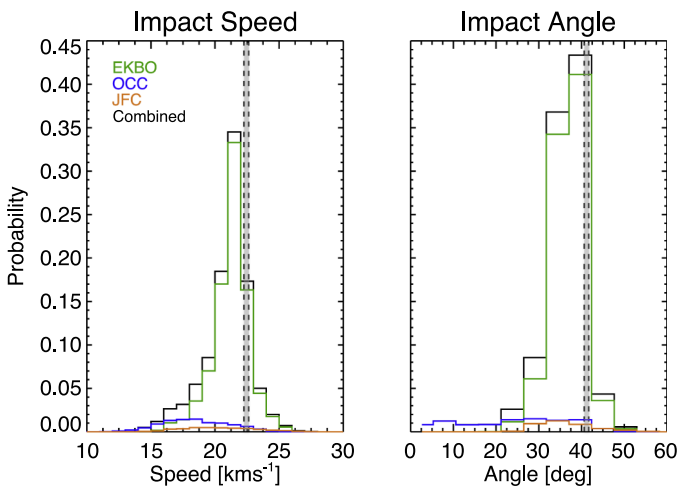


Fig. 11. Speed and angular distribution of 0.6 - 0.85 μm dust grains at 10–11 AU. Shown are the weighted distributions for EKB (green), JFC (orange), and OCC (blue) grains with the combined distribution of all three in black. The range of impact speeds and angles for the assumed circular Kepler orbits, modified by radiation, are shown in gray. Grains following the assumed circular Kepler orbits, modified by radiation pressure, have higher impact speeds and angles than the bulk of the distribution calculated from numerical orbit integrations (Poppe, 2016). (For interpretation of the references to colour in this figure legend, the reader is referred to the web version of this article.)

shallower power law index indicating a distribution with a higher proportion of larger grains.

6. Discussion

The impact charge measured by SDC is a function of both the impact speed and mass of the incoming particle in the charge range of $10^6 < q_{imp} < 10^{10} e^-$ (James et al., 2010). Hence, a customary simplifying assumption is needed to have an independent estimate for the impact speed in order to estimate the mass of an impacting dust particle. With this assumption, the measured impact charge can be turned

into an estimate for the density and size distribution of IDPs along the trajectory of the New Horizons spacecraft. The dust density of grains $> 0.6 \mu\text{m}$ shows an initial increase out to 15 AU then remains fairly constant with a slight dip around 20 AU. The density then begins to increase out to the Kuiper Belt. The density of larger grains ($> 0.9 \mu\text{m}$) remains fairly constant, which is in agreement with Pioneer and Voyager measurements (Humes, 1980; Gurnett et al., 1997; 2005).

Using the combination of SDC and Pioneer 10 dust density measurements, and the results of extensive integration of dust grain trajectories produced in the EKB, the total dust production rate (Poppe, 2016) and the index of an assumed power law initial size distribution (Poppe et al., 2010b; Han et al., 2011; Szalay et al., 2013) can be estimated to match the measurements and the predictions of the numerical models. Curiously, there seems to be a lack of large grains in the SDC data compared to the expectations based on the best fit numerical models. Over all nominal observation periods of spacecraft hibernation, ~ 5.5 years, the largest mass recorded was $\sim 6 \times 10^{-11}$ g. Additionally, grains larger than $\sim 5 \times 10^{-11}$ g have dust counts that are consistent with zero detections, while the model predicts counts on the order of 10 - 50. We have compared the speed and impact angle distributions from the numerical models, and while there are differences, especially in the inner solar system, the effects of these on the mass estimates of impacting IDPs appears to remain modest. It is also possible that the currently available calibration of PVDF sensors is incomplete, and their sensitivity is perhaps changing drastically with impact angle. Alternatively, larger particles ($\geq 5 \times 10^{-11}$ g) may penetrate instead of stopping in the thin PVDF film sensors. Penetrating particles produce smaller charge signals that may be incorrectly identified as smaller grains, thus shifting the mass distribution to smaller sizes (Tuzzolino, 1992). At the same time, the mass estimates from Pioneer 10 might also need revisions (Humes, 1980), providing new constraints on model fits. Finally, the lack of detected large particles could also indicate that their production rate in the EKB and/or lifetime against collisional disruption are overestimated in our current models. As the theoretical models include the effects of collisions, their predictions about densities become a non-linear function of the dust production rate in the EKB, indicating that an updated fit will require a computationally intensive iterative approach.

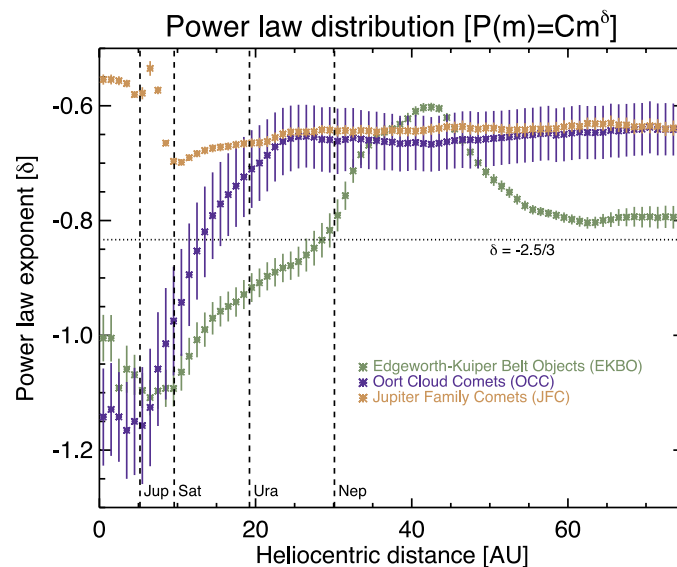


Fig. 12. The fitted power-law index to dust grain densities from Poppe (2016) as a function of heliocentric distance. 1-sigma error bars are included. Included are fits to JFC (orange), OCC (blue), and EKB (green) grains. Locations of Jupiter, Saturn, Uranus, and Neptune are shown as well as a value of $\delta = -0.83$ which is the power-law used as initial production of all sources. (For interpretation of the references to colour in this figure legend, the reader is referred to the web version of this article.)

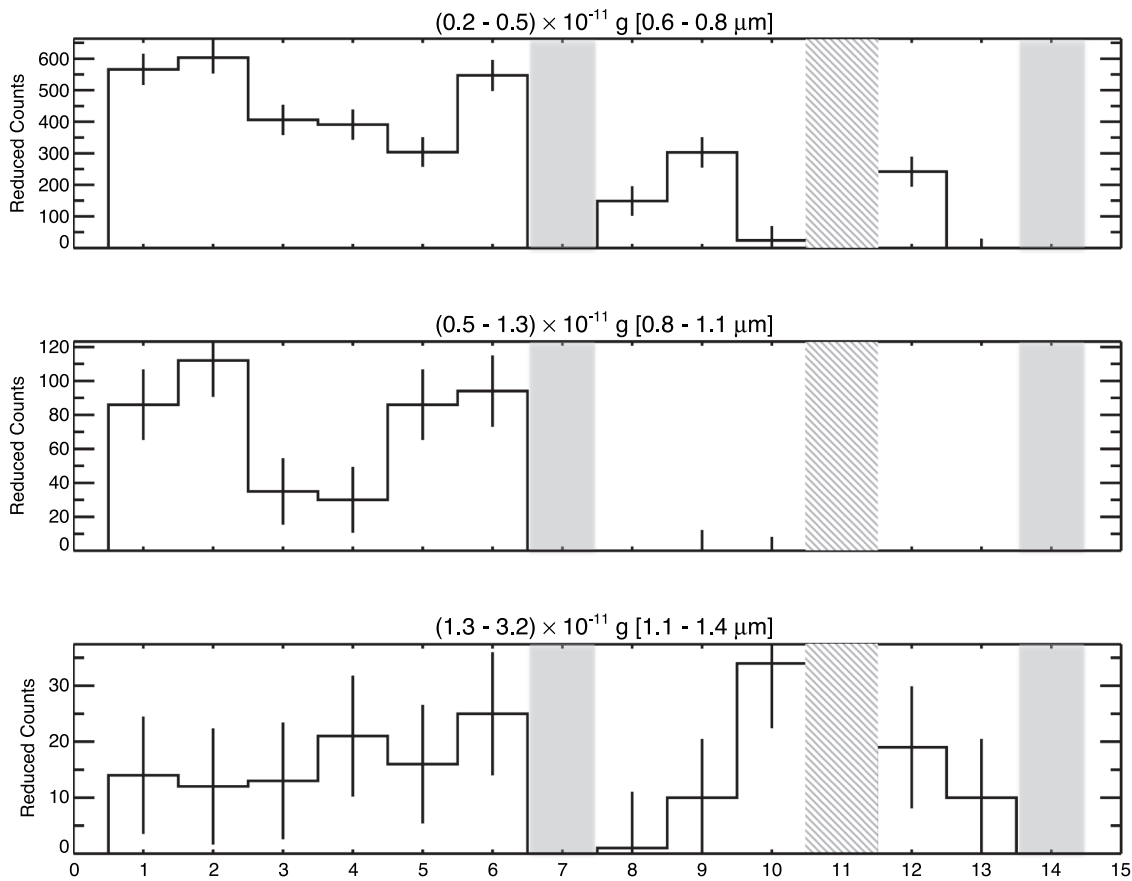


Fig. 13. Reduced dust counts per channel for three logarithmically spaced mass bins. Gray bars indicate reference channels and striped bars indicate channel 11, which died shortly after launch. Error bars were calculated as \sqrt{N} .

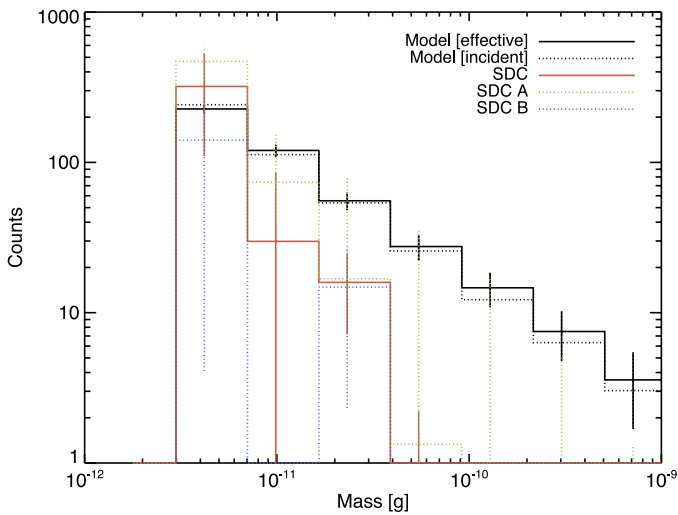


Fig. 14. Modeled incident, modeled effective, and SDC measured mass distributions during all hibernation periods. Error bars were calculated as the standard deviation of the reduced counts for SDC measured distributions and as \sqrt{N} for the modeled distributions.

Acknowledgements

The authors would like to thank the reviewers for their thoughtful feedback and helpful suggestions. This work was supported by NASA’s New Horizons mission. A.R. Poppe was supported by the NASA Planetary Atmospheres program, grant #NNX13AG55G.

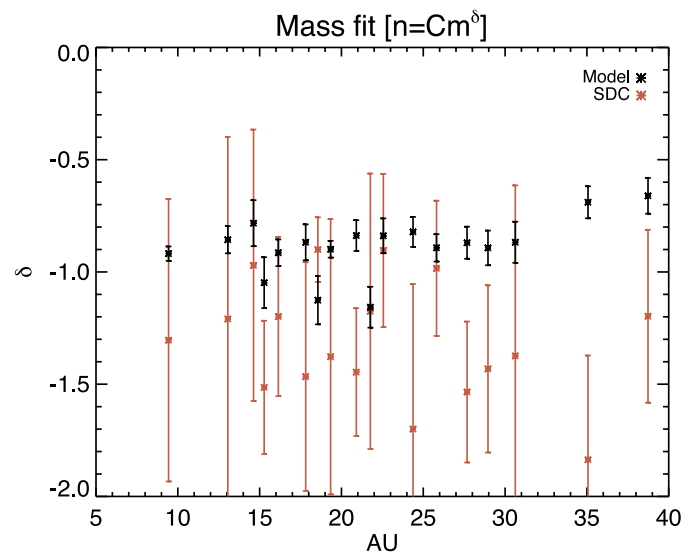


Fig. 15. Predicted and measured impact mass distribution power-law indices during each hibernation period with error bars calculated as the standard error of the fit.

Supplementary material

Supplementary material associated with this article can be found, in the online version, at doi:10.1016/j.icarus.2018.11.012.

References

- Altobelli, N., Dikarev, V., Kempf, S., Srama, R., Helfert, S., Moragas-Klostermeyer, G., Roy, M., Grün, E., 2007. Cassini/Cosmic Dust Analyzer in situ dust measurements between Jupiter and Saturn. *J. Geophys. Res.* 112 (A11), 7105–+. <https://doi.org/10.1029/2006JA011978>.
- Bagenal, F., Horányi, M., McComas, D.J., McNutt, R.L., Elliott, H.A., Hill, M.E., Brown, L.E., Delamere, P.A., Kollmann, P., Krimigis, S.M., Kusterer, M., Lisse, C.M., Mitchell, D.G., Piquette, M., Poppe, A.R., Strobel, D.F., Szalay, J.R., Valek, P., Vandegriff, J., Weidner, S., Zirnstein, E.J., Stern, S.A., Ennico, K., Olkin, C.B., Weaver, H.A., Young, L.A., Team, N.H.S., 2016. Pluto's interaction with its space environment: solar wind, energetic particles, and dust. *Science* 351 (6279), 9045. <https://doi.org/10.1126/science.aad9045>.
- Di Sisto, R.P., Fernández, J.A., Brunini, A., 2009. On the population, physical decay and orbital distribution of Jupiter family comets: numerical simulations. *Icarus* 203 (1), 140–154. <https://doi.org/10.1016/j.icarus.2009.05.002>.
- Dietzel, H., Eichhorn, G., Fechtig, H., Grün, E., Hoffmann, H.-J., Kissel, J., 1973. The HEOS 2 and HELIOS micrometeoroid experiments. *J. Phys. E Sci. Instrum.* 6, 209–217.
- Duncan, M.J., 2008. Dynamical origin of comets and their reservoirs. *Space Sci. Rev.* 138 (1–4), 109–126. <https://doi.org/10.1007/s11214-008-9405-5>.
- Grün, E., Baguhl, M., Fechtig, H., Hanner, M., Kissel, J., Lindblad, B.-A., Linkert, D., Linkert, G., Mann, I., McDonnell, J., 1992a. Galileo and ULYSSES dust measurements - From Venus to Jupiter. *Geophys. Res. Lett.* 19, 1311–1314.
- Grün, E., Fechtig, H., Hanner, M.S., Kissel, J., Lindblad, B.-A., Linkert, D., Maas, D., Morfill, G.E., Zook, H.A., 1992b. The Galileo Dust Detector. *Space Sci. Rev.* 60, 317–340.
- Grün, E., Goertz, C., Morfill, G., Havnes, O., 1992c. Statistics of Saturn's spokes. *Icarus* 99, 191–201. (ISSN 0019-1035), vol.99, no.1, p.191–201.
- Grün, E., Pailer, N., Fechtig, H., Kissel, J., 1980. Orbital and physical characteristics of micrometeoroids in the inner solar system as observed by Helios 1. *Planet. Space Sci.* 28 (3), 333–349. [https://doi.org/10.1016/0032-0633\(80\)90022-7](https://doi.org/10.1016/0032-0633(80)90022-7).
- Gurnett, D.A., Ansher, J.A., Kurth, W.S., Granroth, L.J., 1997. Micron-sized dust particles detected in the outer solar system by the Voyager 1 and 2 plasma wave instruments. *Geophys. Res. Lett.* 24 (24), 3125–3128. <https://doi.org/10.1029/97GL03228>.
- Gurnett, D.A., Wang, Z.Z., Persoon, A.M., Kurth, W.S., 2005. Dust particles detected in the outer Solar System by Voyager 1 and 2. *Dust in Planetary Systems Workshop 2005*. 1280. pp. 63.
- Han, D., Poppe, A.R., Piquette, M., Grün, E., Horányi, M., 2011. Constraints on dust production in the Edgeworth–Kuiper Belt from Pioneer 10 and New Horizons measurements. *Geophys. Res. Lett.* 38, 24102. <https://doi.org/10.1029/2011GL050136>.
- Horányi, M., Hoxie, V., James, D., Poppe, A., Bryant, C., Grogan, B., Lamprecht, B., Mack, J., Bagenal, F., Batiste, S., Bunch, N., Chantawanich, T., Christensen, F., Colgan, M., Dunn, T., Drake, G., Fernandez, A., Finley, T., Holland, G., Jenkins, A., Krauss, C., Krauss, E., Krauss, O., Lankton, M., Mitchell, C., Neeland, M., Reese, T., Rash, K., Tate, G., Vaudrin, C., Westfall, J., 2008. The Student Dust Counter on the New Horizons Mission. *Space Sci. Rev.* 140, 387–402. <https://doi.org/10.1007/s11214-007-9250-y>.
- Humes, D.H., 1980. Results of Pioneer 10 and 11 meteoroid experiments - Interplanetary and near-Saturn. *J. Geophys. Res.* 85, 5841–5852.
- James, D., Hoxie, V., Horányi, M., 2010. Polyvinylidene fluoride dust detector response to particle impacts. *Rev. Sci. Instrum.* 81 (3), 034501. <https://doi.org/10.1063/1.3340880>.
- Krüger, H., Altobelli, N., Anweiler, B., Dermott, S.F., Dikarev, V., Graps, A.L., Grün, E., Gustafson, B.A., Hamilton, D.P., Hanner, M.S., Horányi, M., Kissel, J., Landgraf, M., Lindblad, B.A., Linkert, D., Linkert, G., Mann, I., McDonnell, J.A.M., Morfill, G.E., Polansky, C., Schwehm, G., Srama, R., Zook, H.A., 2006a. Five years of Ulysses dust data: 2000–2004. *Planet. Space Sci.* 54, 932–956. <https://doi.org/10.1016/j.pss.2006.04.015>.
- Krüger, H., Bindschadler, D., Dermott, S.F., Graps, A.L., Grün, E., Gustafson, B.A., Hamilton, D.P., Hanner, M.S., Horányi, M., Kissel, J., Lindblad, B.A., Linkert, D., Linkert, G., Mann, I., McDonnell, J.A.M., Moissl, R., Morfill, G.E., Polansky, C., Schwehm, G., Srama, R., 2006b. Galileo dust data from the Jovian system: 1997–1999. *Planet. Space Sci.* 54, 879–910. <https://doi.org/10.1016/j.pss.2006.04.010>.
- Krüger, H., Dikarev, V., Anweiler, B., Dermott, S.F., Graps, A.L., Grün, E., Gustafson, B.A., Hamilton, D.P., Hanner, M.S., Horányi, M., Kissel, J., Linkert, D., Linkert, G., Mann, I., McDonnell, J.A.M., Morfill, G.E., Polansky, C., Schwehm, G., Srama, R., 2010. Three years of Ulysses dust data: 2005 to 2007. *Planet. Space Sci.* 58 (7), 951–964. <https://doi.org/10.1016/j.pss.2009.11.002>.
- Krüger, H., Grün, E., Graps, A., Bindschadler, D., Dermott, S., Fechtig, H., Gustafson, B.A., Hamilton, D.P., Hanner, M.S., Horányi, M., Kissel, J., Lindblad, B.A., Linkert, D., Linkert, G., Mann, I., McDonnell, J.A.M., Morfill, G.E., Polansky, C., Schwehm, G., Srama, R., Zook, H.A., 2001a. One year of Galileo dust data from the Jovian system: 1996. *Planet. Space Sci.* 49, 1285–1301.
- Krüger, H., Grün, E., Landgraf, M., Baguhl, M., Dermott, S., Fechtig, H., Gustafson, B.A., Hamilton, D.P., Hanner, M.S., Horányi, M., Kissel, J., Lindblad, B.A., Linkert, D., Linkert, G., Mann, I., McDonnell, J.A.M., Morfill, G.E., Polansky, C., Schwehm, G., Srama, R., Zook, H.A., 1999. Three years of Ulysses dust data: 1993–1995. *Planet. Space Sci.* 47, 363–383.
- Krüger, H., Grün, E., Landgraf, M., Dermott, S., Fechtig, H., Gustafson, B.A., Hamilton, D.P., Hanner, M.S., Horányi, M., Kissel, J., Lindblad, B.A., Linkert, D., Linkert, G., Mann, I., McDonnell, J.A.M., Morfill, G.E., Polansky, C., Schwehm, G., Srama, R., Zook, H.A., 2001b. Four years of Ulysses dust data: 1996–1999. *Planet. Space Sci.* 49, 1303–1324. [https://doi.org/10.1016/S0032-0633\(01\)00054-X](https://doi.org/10.1016/S0032-0633(01)00054-X).
- Krüger, H., Linkert, G., Linkert, D., Moissl, R., Grün, E., 2005. Galileo long-term dust monitoring in the Jovian magnetosphere. *Planet. Space Sci.* 53, 1109–1120. <https://doi.org/10.1016/j.pss.2005.04.009>.
- Kuchner, M.J., Stark, C.C., 2010. Collisional Grooming Models of the Kuiper Belt Dust Cloud. *Astrophys. J.* 140, 1007–1019. <https://doi.org/10.1088/0004-6256/140/4/1007>.
- Landgraf, M., Liou, J.-C., Zook, H.A., Grün, E., 2002. Origins of Solar System Dust beyond Jupiter. *Astrophys. J.* 123, 2857–2861. <https://doi.org/10.1086/339704>.
- Levison, H.F., Duncan, M.J., 1997. From the Kuiper Belt to Jupiter-Family Comets: the Spatial Distribution of Ecliptic Comets. *Icarus* 127 (1), 13–32. <https://doi.org/10.1006/icar.1996.5637>.
- Liou, J.-C., Zook, H.A., 1999. Signatures of the Giant Planets Imprinted on the Edgeworth–Kuiper Belt Dust Disk. *Astron. J.* 118 (1), 580. <https://doi.org/10.1086/1006/1996.5637>.
- Liou, J.-C., Zook, H.A., Dermott, S.F., 1996. Kuiper Belt Dust Grains as a Source of Interplanetary Dust Particles. *Icarus* 124, 429–440. <https://doi.org/10.1006/icar.1996.0220>.
- Liou, J.-C., Zook, H.A., Jackson, A.A., 1999. Orbital evolution of retrograde Interplanetary Dust Particles and their distribution in the Solar System. *Icarus* 141, 13–28. <https://doi.org/10.1006/icar.1999.6170>.
- Moro-Martín, A., Malhotra, R., 2002. A study of the dynamics of dust from the Kuiper Belt: spatial distribution and spectral energy distribution. *Astron. J.* 124, 2305–2321. <https://doi.org/10.1086/342849>.
- Moro-Martín, A., Malhotra, R., 2003. Dynamical models of Kuiper Belt Dust in the inner and outer Solar System. *Astrophys. J.* 125, 2255–2265. <https://doi.org/10.1086/368237>.
- Nesvorný, D., Janches, D., Vokrouhlický, D., Pokorný, P., Bottke, W.F., Jenniskens, P., 2011. Dynamical model for the Zodiacal Cloud and Sporadic Meteors. *Astrophys. J.* 743 (2), 129. <https://doi.org/10.1088/0004-637X/743/2/129>.
- Nesvorný, D., Jenniskens, P., Levison, H.F., Bottke, W.F., Vokrouhlický, D., Gounelle, M., 2010. Cometary origin of the Zodiacal Cloud and Carbonaceous Micrometeorites. Implications for Hot Debris Disks. *Astron. J.* 713, 816–836. <https://doi.org/10.1088/0004-637X/713/2/816>.
- Petit, J.-M., Kavelaars, J.J., Gladman, B.J., Jones, R.L., Parker, J.W., Laerhoven, C.V., Nicholson, P., Mars, G., Rousselot, P., Mousis, O., Marsden, B., Bieryla, A., Taylor, M., Ashby, M.L.N., Benavidez, P., Bagatin, A.C., Bernabeu, G., 2011. The Canada–France Ecliptic Plane Survey—full data release: the orbital structure of the Kuiper Belt. *Astron. J.* 142 (4), 131. <https://doi.org/10.1088/0004-6256/142/4/131>.
- Poppe, A., Jacobsmeyer, B., James, D., Horányi, M., 2010a. Simulation of polyvinylidene fluoride detector response to hypervelocity particle impact. *Nuclear Instrum. Methods Phys. Res. A* 622, 583–587. <https://doi.org/10.1016/j.nima.2010.07.088>.
- Poppe, A., James, D., Horányi, M., 2011. Measurements of the terrestrial dust influx variability by the Cosmic Dust Experiment. *Planet. Space Sci.* 59, 319–326. <https://doi.org/10.1016/j.pss.2010.12.002>.
- Poppe, A., James, D., Jacobsmeyer, B., Horányi, M., 2010b. First results from the Venetia Burney Student Dust Counter on the New Horizons mission. *Geophys. Res. Lett.* 37, 11101. <https://doi.org/10.1029/2010GL043300>.
- Poppe, A.R., 2015. Interplanetary dust influx to the Pluto–Charon system. *Icarus* 246, 352–359. <https://doi.org/10.1016/j.icarus.2013.12.029>.
- Poppe, A.R., 2016. An improved model for the interplanetary dust fluxes in the outer solar system. *Icarus* 264, 369–386.
- Simpson, J.A., Tuzzolino, A.J., 1985. Polarized polymer films as electronic pulse detectors of cosmic dust particles. *Nucl. Instrum. Methods A* 236, 187–202.
- Srama, R., Ahrens, T.J., Altobelli, N., Auer, S., Bradley, J.G., Burton, M., Dikarev, V.V., Economou, T., Fechtig, H., Görlich, M., Grande, M., Graps, A., Grün, E., Havnes, O., Helfert, S., Horányi, M., Igenbergs, E., Jessberger, E.K., Johnson, T.V., Kempf, S., Krivov, A.V., Krüger, H., Mocker-Ahlrepp, A., Moragas-Klostermeyer, G., Lamy, P., Landgraf, M., Linkert, D., Linkert, G., Lura, F., McDonnell, J.A.M., Möhlmann, D., Morfill, G.E., Müller, M., Roy, M., Schäfer, G., Schlotzauer, G., Schwehm, G.H., Spahn, F., Stübig, M., Svestka, J., Tschernjawski, V., Tuzzolino, A.J., Wäsch, R., Zook, H.A., 2004. The Cassini Cosmic Dust Analyzer. *Space Sci. Rev.* 114, 465–518. <https://doi.org/10.1007/s11214-004-1435-z>.
- Stark, C.C., Kuchner, M.J., 2009. A new algorithm for self-consistent three-dimensional modeling of collisions in Dusty Debris Disks. *Astrophys. J.* 707 (1), 543. <https://doi.org/10.1088/0004-637X/707/1/543>.
- Stern, S.A., 1996. Signatures of collisions in the Kuiper Disk. *Astron. Astrophys.* 310, 999–1010.
- Szalay, J.R., Piquette, M., Horányi, M., 2013. The Student Dust Counter: status report at 23 AU. *Earth Planets Space* 65 (10), 1145–1149.
- Tuzzolino, A.J., 1992. PVDF copolymer dust detectors: particle response and penetration characteristics. *Nuclear Instrum. Methods Phys. Res. A* 316, 223–237. [https://doi.org/10.1016/0168-9002\(92\)90904-I](https://doi.org/10.1016/0168-9002(92)90904-I).
- Vitense, C., Krivov, A.V., Kobayashi, H., Löhne, T., 2012. An improved model of the Edgeworth–Kuiper debris disk. *Astron. Astrophys.* 540, A30. <https://doi.org/10.1051/0004-6361/201118551>.
- Vitense, C., Krivov, A.V., Löhne, T., 2014. Will New Horizons see dust clumps in the Edgeworth–Kuiper Belt? *Astrophys. J.* 147, 154. <https://doi.org/10.1088/0004-6256/147/6/154>.
- Wehry, A., Mann, I., 1999. Identification of β -meteoroids from measurements of the dust detector onboard the ULYSSES spacecraft. *Astron. Astrophys.* 341, 296–303.
- Yamamoto, S., Mukai, T., 1998. Dust production by impacts of interstellar dust on Edgeworth–Kuiper Belt objects. *Astron. Astrophys.* 329, 785–791.
- Zook, H.A., 1975. Hyperbolic cosmic dust: its origin and its astrophysical significance. *Planet. Space Sci.* 23 (10), 1391–1397. [https://doi.org/10.1016/0032-0633\(75\)90034-3](https://doi.org/10.1016/0032-0633(75)90034-3).
- Zook, H.A., Berg, O.E., 1975. A source for hyperbolic cosmic dust particles. *Planet. Space Sci.* 23 (1), 183–203. [https://doi.org/10.1016/0032-0633\(75\)90078-1](https://doi.org/10.1016/0032-0633(75)90078-1).